

# The effect of gravity on turbulent, primixed flame propagation - A preliminary cold flow study

**M. Disseau**

*Georgia Inst. of Technology, Atlanta*

**S. Menon**

*Georgia Inst. of Technology, Atlanta*

**J. Jagoda**

*Georgia Inst. of Technology, Atlanta*

**R. Sujith**

*Georgia Inst. of Technology, Atlanta*

**AIAA, Aerospace Sciences Meeting & Exhibit, 35th, Reno, NV, Jan. 6-9, 1997**

The effect of buoyancy is removed from a turbulent Couette flow by testing it under conditions of microgravity. The velocity field of the cold flow under normal gravity forces is fully characterized. The feasibility of using acetone planar laser induced fluorescence to measure turbulent passive scalar diffusion is confirmed. It is determined that the full range of turbulence scales can be observed experimentally for Reynolds numbers of interest in subsequent combustion studies. (Author)



scale. Their magnitudes change, relative to each other, with  $Re_L$  by the relation

$$L / \eta = (Re_L)^{3/4} \quad (1)$$

This implies that for a given  $L$ , which is the case in most experimental flow fields, low Reynolds numbers ensure relatively large Kolmogorov scales, making them easier to measure. However, turbulence in practical devices is usually associated with high Reynolds numbers. An additional problem is encountered when trying to simulate a high Reynolds number reacting flow by a flow with low Reynolds number. At high Reynolds numbers large scale turbulent stresses are responsible for momentum transport. These stresses, however, can be overwhelmed by buoyancy forces in lower Reynolds number flows.

To remove the effect of buoyancy in a low Reynolds number turbulent reacting flow field a microgravity environment is required. As stated by King<sup>3</sup> microgravity has numerous benefits in combustion science including, but not limited to: increased scalar resolution by allowing the use of larger scales, truly one dimensional geometries, or at least geometries not deformed by buoyancy, and more uniform flames, since buoyancy is temperature dependent, and thus affects different areas of the flame differently. This enables a more accurate study of the combustion processes, which leads to an increased understanding of turbulent combustion.

A Couette flow configuration was selected to generate a turbulent flow at relatively low Reynolds numbers for this study. A Couette flow is a classical shear layer flow produced between two parallel plates moving in opposite directions each at a fixed velocity  $U_{wall}$ . This flow has the benefit that the shear stress is constant though-out the cross-section, and that the intensity of turbulent fluctuation is constant for most of the cross-section. Due to these and other characteristics, Couette flow has been widely studied over the years<sup>4,5,6,7</sup>. In addition, such a flow can be generated in the confined space available in the drop tower facility described below.

The NASA Lewis 2.2 Second Drop tower was chosen as the site of the microgravity experiments. This facility allows a 40.64cm by 96.52cm by 83.82cm experimental rig to experience 2.2 seconds of  $\sim 10^{-4}g$  followed by 0.2 sec deceleration (at 15 to 30 g). Due to the spatial and temporal restriction imposed by this experimental facility<sup>8</sup> the diagnostic techniques of choice, like laser Doppler velocimetry (LDV), cannot

be used to study the flow field. To interpret the results from more basic diagnostic techniques, like OH fluorescence and Schlieren imaging, it is essential to fully understand the non-reacting flow field. Two techniques were used to date to characterize the non-reacting flow field. The velocity and shear flow field was mapped for different flow conditions using LDV. In addition turbulent diffusion of passive species are being visualized using acetone planar laser induced fluorescence (PLIF). This technique is used to measure the scales of the flow so as to determine the required resolution for future combustion visualization techniques. This paper will report the results of the cold flow study, and discuss the resulting requirements for the combustion experiments.

### Experimental Facility

The experimental device used in this study is shown in Fig. 1. The device consists of a continuous Mylar belt ① which provides the "two parallel plates" moving in opposite directions. The belt runs over a series of rollers, two of which drive the belt while four are used

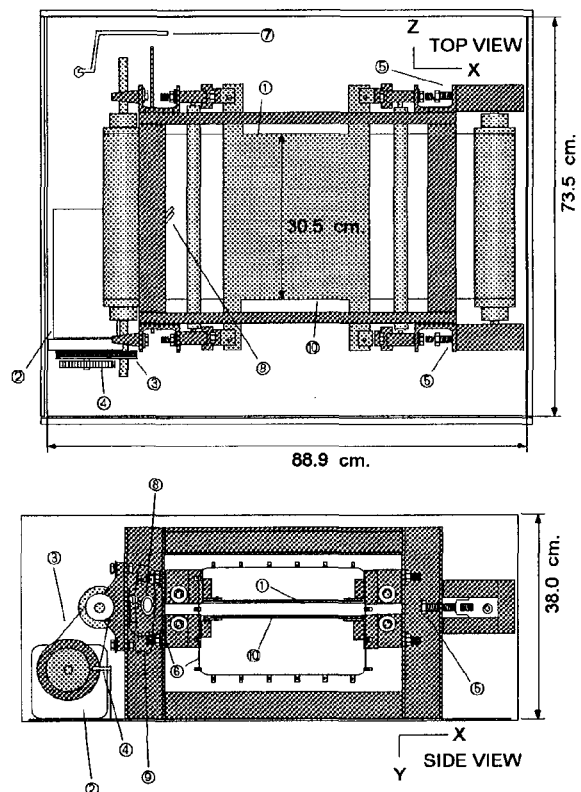


Figure 1- Current setup of the experimental device. Call-outs described in the text.

to adjust the spacing in the test section. It is driven by an adjustable DC motor ② connected to the drive roller by a set of pulleys and a v-belt ③. The rotational speed of the motor is sensed by a magnetic proximity sensor ④. Knowing the pulley ratio and the roller diameter, the speed of the belt can easily be determined. To prevent belt walking and to ease the insertion of a new belt, a set of tensioning screws ⑤ help position the far roller. The Reynolds number for the device,  $Re_h$ , can be changed by either changing the speed of the belt,  $U_{belt}$ , or by changing the belt spacing,  $h$ . The device is surrounded by a Plexiglas box to prevent any external influence on the flow without disturbing optical access to the experiment.

Because of the restrictions of the drop tower the device used in this study had to be more compact than those used in other Couette flow studies. A survey by Aydin *et al.*<sup>4</sup> shows that the current device has the smallest gap spacing, 2.54cm versus 3 to 12cm, the smallest length to gap ratio, 14 versus 30 to 158, and one of the smallest width to gap ratio, 12 versus 7 to 28, of air Couette devices. In addition, the current device operates in a closed loop, i.e. turbulent flow is forced to recenter the test section. Most other studies were carried in devices which, in essence, transition the flow from laminar to turbulent. As a result the flow field generated by the device developed for this study had to be extensively studied and the extent to which it deviates from an ideal Couette flow had to be documented.

The velocity flow field was mapped with a TSI 9100-7 two component laser Doppler velocimeter, which uses the 514.5nm and 488nm wavelengths of an 5 watt  $Ar^+$  laser. After going through an expander and focusing using a 14mm aperture lens, with a 750mm focus, the probe volume was 0.13mm in diameter and 1.3mm long. The system was used in back scatter mode. The output signals were analyzed by a TSI IFA656 digital burst correlator, which can cope with lower signal to noise ratios than a traditional counter. One beam of each pair was frequency shifted by a Bragg cell to allow for measurement of negative velocities. Big central glass windows ⑥ were installed in the enclosure because it was soon discovered that the Plexiglas box absorbs too much light, and thus renders the scattered signal too faint. In order to avoid cutting off one of the two beams used to measure the velocity component normal to the belt the device was slightly tilted. The tilt angle was measured by plain geometry, using a HeNe laser as a pointer. Sub-micron  $TiO_2$  particles were used to seed the flow. After passing through a fluidized bed,  $TiO_2$  laden air is inserted into

the device through a tube ⑦, which produces a cloud of seed around the moving belts that is then entrained into the Couette flow. This eliminates the possibility of biasing the data with artificial seeding velocities. FIND software, from TSI, was then used to statistically process the 50,000 samples obtained at each location. Data was velocity bias corrected according to the algorithm provided in FIND.

As discussed below early velocity data showed that the flow field between the belt is two dimensional. However a spectral analysis of the velocity data showed that the belt was vibrating. The vibrations were minimized by adding plates ⑧ on the outside of the belt.

Acetone PLIF is performed using a tunable Lambda Physik excimer laser running with KrF, to produce a laser pulse at a wavelength of 248nm. The beam is used to create a sheet which enters through the quartz window ⑨. It penetrates in-between the Mylar sheets through a cut in the frame ⑩, and is turned by a mirror ⑪, to run along the mean flow direction. A micro-tube 0.254mm in diameter and with a hole cut in its side, is positioned perpendicular to the flow. Liquid acetone is introduced through the tube into the center of the flow. Here a droplet of acetone stays suspended in the flow while it vaporizes. When the excimer beam encounters the acetone vapor the latter fluoresces broadband in the blue (350-550nm), with peaks at 445nm and 480nm. The fluorescence is tracked with a Princeton Instruments Inc. intensified camera with a resolution of 384x576 pixels. At this resolution the camera can operate at a rate of two frames per second. The rate can be increased by decreasing the resolution, yielding 10 frames per seconds with a resolution of 192x288 pixels, and 20 frames per second with a resolution of 96x144 pixels.

A 55mm macro glass lens is used on the camera in order to absorb any scattered UV light from the beam. Images are background corrected to remove noise created by fluorescence due to UV scattering off parts of the device. This fluorescence is very prominent close to the belt and close to the needle. Therefore, these regions are not imaged.

## Results

### Velocity Field Mapping

Figure 2 shows the velocity distribution and, therefore the two dimensionality of the flow. The  $z/w = 0$

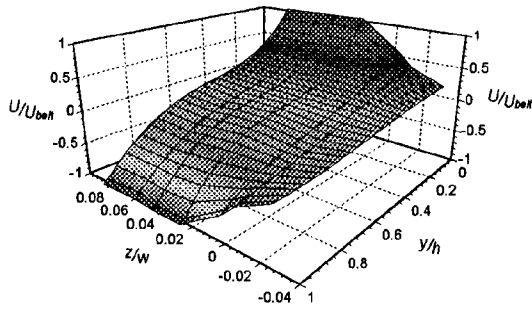


Figure 2 - Velocity distribution showing two dimensionality of the flow. This test was performed at the beginning of the project at a  $Re_h = 2100$ .

location corresponds to the edge of the belt. It can be seen that the velocity profile is constant for  $z/w$  up to 0.04, which corresponds to 1.2cm, from this edge. This yields a usable, two-dimensional test area that is 28.0cm wide. As a result most velocity data were obtained 2cm off-center, which gave better optical access.

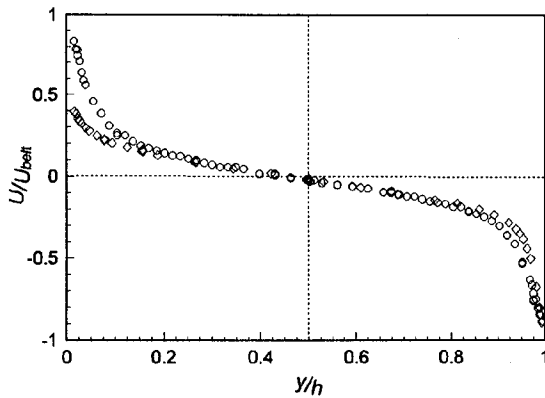


Figure 3 - Velocity distribution across the flow  $\diamond Re_h = 10,091$ ,  $\circ Re_h = 4,366$ .

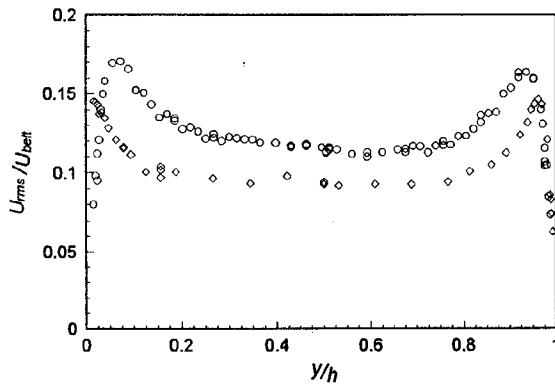


Figure 4 - Turbulent velocity fluctuation distribution across the flow:  $\diamond Re_h = 10,091$ ,  $\circ Re_h = 4,366$ .

Figure 3 shows the velocity distribution across the flow field. Careful inspection of this plot shows that the velocity profile is not totally symmetric. The  $U$  component of velocity should go through zero at  $y/h = 0.5$ , but in reality it does so at  $y/h = 0.45$ . It was hypothesized that this was due to an asymmetry in the end regions where the driving rollers are located. To prove this the motor was set in reverse and, as expected, the crossing moved to  $y/h = 0.55$ . This feature does not seem to have any affect on the rms velocity as seen in Fig. 4, and as long as it is kept in mind while analyzing the combustion data, it is not deemed to be a problem.

As mentioned in the experimental section, there was a slight fluttering of the belt during early testing. This flutter was not visible to the naked eye, but was detected by frequency analysis of the velocity spectrum. A non-excited frequency spectrum should decay smoothly. The excited frequency spectrum that was encountered had peaks in the 100 Hz region, as shown in Fig. 5. A microphone was placed in the flow to check whether corresponding pressure oscillations

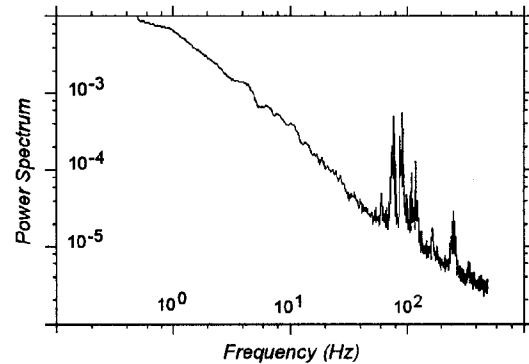


Figure 5 - Frequency spectrum for the case without plates.

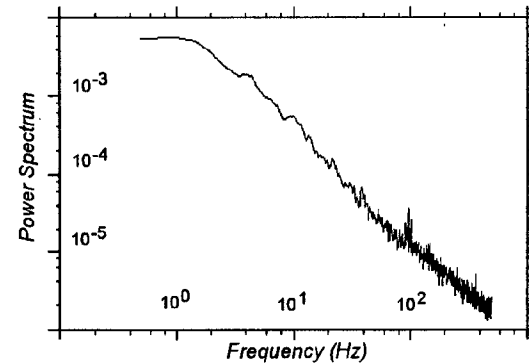


Figure 6 - Frequency spectrum for worst case with plates.

were encountered at that frequency, and they were. These oscillation were increasing the turbulence intensity, but their frequency was dependent on the belt tension, which could not be accurately measured or reproduced. Thus this situation was deemed unacceptable. With the plates in position the fluctuation were almost stopped completely. Figure 6 shows the worst case encountered where the oscillations were not fully damped.

To discuss the results further the following quantities have to be introduced. The shear stress  $\tau_{ij}$  is given by

$$\tau_{ij} = \mu \left( \frac{\partial U_i}{\partial x_j} + \frac{\partial U_j}{\partial x_i} \right) - \rho \overline{(u_i u_j)} \quad (2)$$

The first term represents the viscous stresses and the second represents the Reynolds stresses. In a pure Couette flow the shear stress is constant; though the Reynolds stresses are mainly concentrated in the center of the flow, and the viscous stresses are mainly present near the wall. Another useful quantity is the shear velocity  $U^*$

$$U^* = \left( \frac{\tau_{wall}}{\rho} \right)^{1/2} \quad (3)$$

The velocity and positions in the flow field are commonly non-dimensionalized as follows:

$$U^+ = \frac{U}{U^*} \quad V^+ = \frac{V}{U^*} \quad (4)$$

$$U_{rms}^+ = \frac{U_{rms}}{U^*} \quad V_{rms}^+ = \frac{V_{rms}}{U^*} \quad (5)$$

$$y^+ = \frac{yU^*}{\nu} \quad (6)$$

Figure 7 shows  $U^+$  as a function of  $y^+$ . The data clearly show the expected behavior for a wall bounded shear flow. The flow can be divided into two regions<sup>10</sup>, the viscous sublayer ( $y^+ < 5$ ), and the inertial sublayer ( $30 < y^+ < 1000$ ). The flow correlates well with the linear behavior at the wall in the viscous sublayer. The logarithmic behavior in the inertial sublayer is also clearly present. However the data at different Reynolds numbers do not exactly collapse into one single line when non dimensionalized, as predicted by theory and seen by others. This is probably due to the smaller dimensions and re-circulating nature of the present device.

Figure 8 shows  $U_{rms}^+$  and  $V_{rms}^+$  as functions of non-dimensional distance from the belt. As expected,  $U_{rms}^+$  has a turbulence peak close to the wall before it reaches a uniform distribution in the core, and  $V_{rms}^+$  gradually increases to a uniform distribution in the core. Figure 9 shows how velocity fluctuations vary

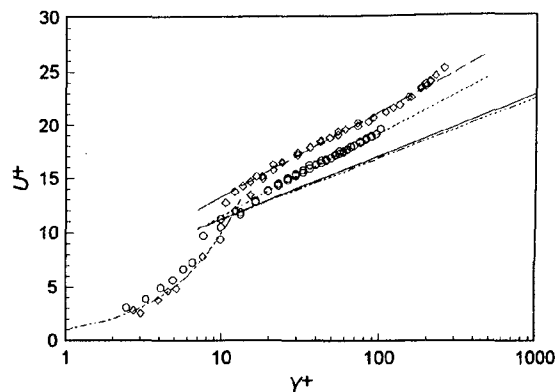


Figure 7 - Non-dimensionalized mean flow velocities and their curve fits:  $\diamond Re_h = 10,091$ ,  $\circ Re_h = 4,366$ ,  $\cdots Y^+ = U^+$ ,  $- - U^+ = 5.4 + 3.4 \ln Y^+$  and  $\cdot \cdot U^+ = 3.9 + 3.3 \ln Y^+$  for present study;  $- \cdot U^+ = 5.2 + 2.55 \ln Y^+$  for El Telbany *et al.*<sup>6</sup>;  $- - - U^+ = 5.6 + 2.43 \ln Y^+$  for Robertson *et al.*<sup>7</sup>; and  $- \cdot U^+ = 5.5 + 2.5 \ln Y^+$  for Aydin *et al.*<sup>4</sup>.

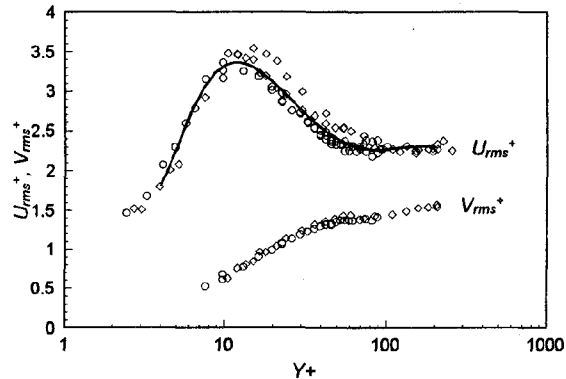


Figure 8 - Non- dimensionalized turbulent velocity fluctuation for present study:  $\diamond Re_h = 10,091$ ,  $\circ Re_h = 4,366$ .

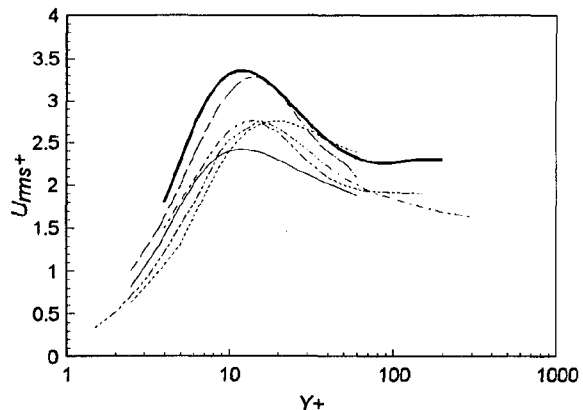


Figure 9 - Non-dimensionalized turbulent velocity fluctuation:  $\cdots$  Aydin *et al.*<sup>4</sup>,  $-$  Clark<sup>2</sup>,  $- \cdot$  El Telbany *et al.*<sup>6</sup>,  $- - -$  Hussain *et al.*<sup>6</sup>,  $- \cdot$  Robertson *et al.*<sup>4</sup>,  $-$  present study.

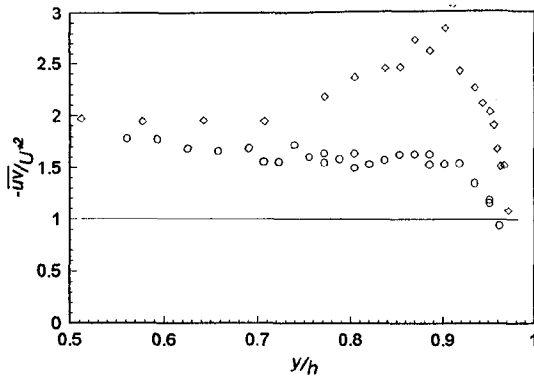


Figure 10 - Non-dimensionalized Reynolds stresses for present study:  $\diamond Re_h = 10,091$ , and  $\circ Re_h = 4,366$ .

for different devices. Except for Clark's device, which was actually not a Couette, but a channel flow, it would seem that the flow in this device is more turbulent than those in other devices. This feature is also seen by looking at the Reynolds stresses.

It is convention to non-dimensionalize Reynolds stresses by  $U^{*2}$ . Inspection of Equations (2) and (3), and the velocity profile, shows that in theory the non-dimensional Reynolds stress should level out at a value of 1. Figure 10 shows that in this flow the turbulent stresses are higher than expected in a pure Couette flow. This is an advantage in this case since higher turbulence is produced at lower Reynolds numbers. In addition, a peak in Reynolds stress near the wall is seen at the higher Reynolds number. Such a peak has not been reported anywhere in the literature.

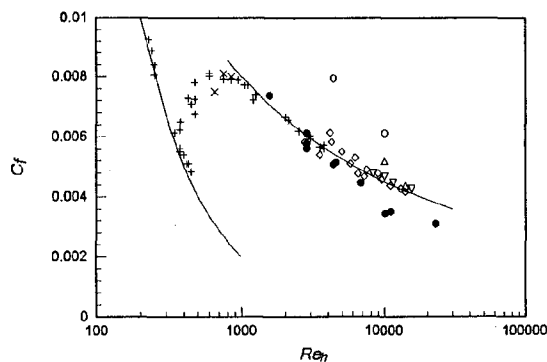


Figure 11 - Coefficient of Friction: + Couette in water<sup>7</sup>, x Couette in air<sup>7</sup>, Δ Robertson in air (center)<sup>7</sup>, ∇ Robertson in air (wall)<sup>7</sup>, ◇ Robertson and Johnson in air<sup>7</sup>, ● present study in air (wall), and ○ present study in air (center).

A way of quantifying the shear stresses is by measuring the coefficient of friction.

$$C_f = \frac{\tau_{ij}}{\frac{1}{2}\rho U_{wall}^2} \quad (7)$$

In general the coefficient of friction is more meaningful at the wall, and thus usually represents the viscous stresses. Since in pure Couette flow there is a uniform shear, the coefficient of friction measured at the center is supposed to yield the same approximate answer as the coefficient of friction measured at the wall. Figure 11 shows the coefficient of friction measured in this device compared to those in previous investigated Couette flows.  $C_f$  calculated from the center measurements of shear stress for this flow field are higher than the ones calculated at the wall. This is due to the higher than expected Reynolds stresses. Deviations from more ideal Couette flow are, once again, probably due to the recirculating nature of the flow in this compact device.

A parallel computational study of this flow assumes the existence of an inertial range in which the flow follow the  $k^{-5/3}$  law. The experimental validation of this assumption requires the determination of a wave number spectra for this flow. Since LDV measurements are single point, wave number spectra can only be obtained from frequency spectra using Taylor's hypothesis<sup>11</sup>. One of the criteria for Taylor's hypothesis to hold is that  $U/U_{rms} \gg 1$ . This is clearly not the case, in what can be considered the inertial range of this device. However, it might still be interesting to examine the wavelength spectra to obtain some qualitative information, while keeping in mind the assumptions made in calculating the spectra.

Following Taylor's hypothesis a wave number can be defined as follows<sup>9</sup>:

$$k_1 = \frac{2\pi f}{U} \quad (8)$$

The absolute value of spectral density in wave number space is given as:

$$\phi_{u_{ii}} = \frac{f \overline{u_i^2(f)}}{k_1 y U^*} \quad (9)$$

If one now plots  $\phi_{u_{ii}}$  versus  $k_1 y$ , where  $y$  is the position from the wall, one can look at spectra for different regions in the flow and note which ones follow the  $k^{-5/3}$  law.

Figure 12 shows  $\phi_{u_{11}}(k_1)$  and  $\phi_{u_{22}}(k_1)$  versus  $ky$  for different regions in the flow. These velocity spectra are for the case of  $Re_h=10,091$ . The  $U$ , and  $V$  spectra for

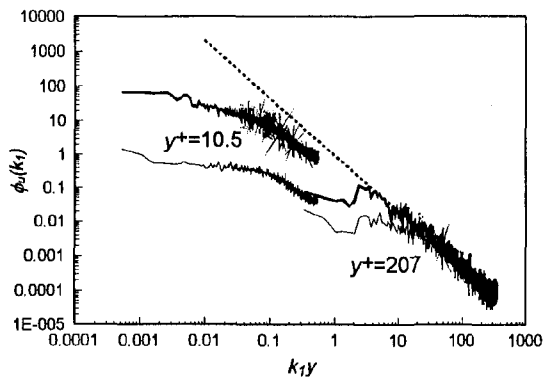


Figure 13 - Wave number spectral analysis: —  $\phi_{u_{11}}(k_1)$   
 —  $\phi_{u_{22}}(k_1)$ , ..  $k^{-5/3}$ .

the  $y^+ = 207$  location follow the inertial layer law, but those for the  $y^+ = 10.5$  location do not. As a matter of fact the inertial behavior can only be seen in spectra for the  $y^+ > 60$  locations, which correspond to the region of constant  $U_{rms}$ . Thus the assumption of the existence of an inertial layer necessary for the parallel computational study is valid in the region of interest.

Visualization of Turbulent Diffusion

The hypodermic needle carrying the acetone drop was placed below the centerline where the flow runs from right to left. The fluorescence of the acetone in the region to the left of the needle was recorded. Flow in the lower half of the picture is expected to be acetone laden, while flow in the upper half of the picture is expected to be free of acetone. Figure 13 shows a snapshot of the resulting turbulent diffusion process. The light marking correspond to the presence of acetone. As expected high concentration of acetone is seen in the lower half of the image. Some large scales structures can be seen in this picture. It is not certain whether these are Couette flow structures or whether vortices are shed off the acetone supply line. The Reynolds number based on the diameter of the needle is of the order of 10, thus it is safe to assume that the needle does not produce structures. However the Reynolds number associated with the droplet is of the order of 150, thus making it very possible for it to shed vortices.

For the feasibility study reported here, the fluorescence measurements of acetone were carried out under steady conditions. In order to better determine the influence of turbulent passive scalar diffusion processes, it will be necessary to observe the leading edge of the acetone as it begins to diffuse into the flow. This will require a

higher framing rate and a more sophisticated timing of the injector and camera, which are under preparation. However, the test reported here did show that it is possible to visualize diffusion in this flow using acetone PLIF.

Considerations on the Resolution of Scales

One of the premises of this study was the need to have access to a wide range of scales, to allow a better understanding of the turbulent combustion process. It is, therefore, important to consider the ability of the cold flow study to resolve these scales. As mentioned in the introduction  $L$ , the integral length scale, can be approximated as the significant length scale in the flow, which in this case is the belt spacing,  $h$ , and equals 25.4mm. The Kolmogorov scale,  $\eta$ , can be calculated from Equation (1) where the Reynolds number is determined from the turbulent velocities measured in the core of the flow. They were found to be 0.23mm for the  $Re_h = 4,366$  case and 0.13mm for the  $Re_h = 10,091$  case.

Considerations for LDV: The integral length scale can definitively be resolved by measuring full traverses with the LDV. The Kolmogorov scale, on the other hand needs to be more carefully considered. The seed particle size is sub-micron, much smaller than  $\eta$ , while the LDV probe volume is of the order of the  $\eta$ . This implies that the scale can just be spacially resolved during two point correlation measurements. However smaller scales may be temporally resolved. Since the scales are moving, residence time inside the probe volume is a more accurate measurement of scale resolution. The velocity of the scale can be estimated by using the relation between Kolmogorov velocity scale and the magnitude of turbulent velocity:

$$u' / \nu = (Re_t)^{1/4} \tag{10}$$

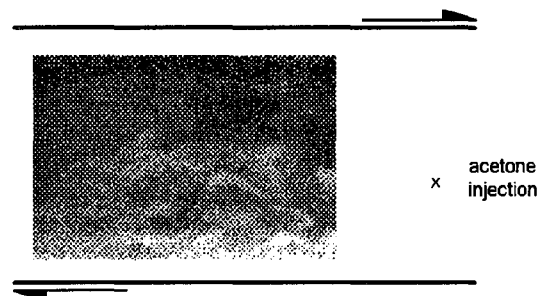


Figure 12 - Picture of acetone PLIF signal. The light regions correspond to the presence of acetone in the flow. To the right of the picture is acetone injection system. The arrows correspond to direction the belt is moving in.

Based on the probe volume dimensions and Equation (10) a residence time and, therefore, a frequency can be calculated to be 590Hz for the  $Re_h = 4,366$  case and 1,030Hz for the  $Re_h = 10,091$  case. This means that the data rate for the LDV should be greater than 2,060Hz to resolve Kolmogorov scales temporally. Because of the high noise levels in the system, this is difficult to achieve. It thus requires considerable attention to alignment and seeding to obtain information on the smallest scales in the flow.

Consideration for PLIF: Again the integral length scale can be resolved without a problem. On the other hand, the full resolution of the camera combined with the macro lens used yields a pixel dimension of 0.05 mm squared. This results in approximately  $3 \times 3$  pixels per Kolmogorov scale, for  $Re_h = 10,091$ , and  $5 \times 5$  pixels per Kolmogorov scale for  $Re_h = 4,366$ . Decreased resolution to achieve higher frame rates would of course decrease these estimates. However, reduced areas of interest can be viewed with higher magnification lenses, which would increase the resolution significantly.

#### Combustion Considerations

The wrinkledness of a turbulent premixed flame depends upon the ratio between the turbulent velocity fluctuation and the laminar flame speed. In the  $Re_h = 10,091$  flow the core has a  $U_{rms}$  of 0.75 m/sec, which is 4 times bigger than the laminar flame speed for lean limit methane air combustion. Since this Reynolds number also lies at the limit of the Kolmogorov scale resolution, most test will be carried out under this flow regime.

#### Conclusions

A facility in which Couette like, non-reacting and reacting flows could be generated in a microgravity environment was designed and built. To fit into the NASA Lewis drop tower the device has to be very compact. This means that edge effects and flow re-circulation were expected to affect the flow.

The flow field was thoroughly investigated using laser Doppler velocimetry. The flow was found to be largely two dimensional with constant turbulence intensities near the core. Slight flow asymmetries are introduced by the non symmetric re-circulation of the fluid outside the test region. Belt flutter problems were remedied by adding a pair of guide plates to the belt. In general the flow field was found to be quite similar to previously

investigated Couette flows. However, turbulence levels and associated shear stresses were higher. This is probably due to the confined re-circulation zone reintroducing turbulence into the test section.

The feasibility of measuring turbulent scalar diffusion in the Couette flow was confirmed by suspending droplets of acetone and visualizing their acetone vapor as it diffuses in the flow by planar laser induced fluorescence. Turbulence scales were compared with the spatial and temporal resolution of the experimental techniques and it was determined that for Reynolds numbers of about 10,000 structures down to the Kolmogorov scale could be resolved.

#### Acknowledgments

This Research was sponsored by a grant (No. NAG 3-1610) from the NASA Lewis Research Center. The authors wish to recognize the support provided by the staff of the Aerospace Combustion Laboratory at Georgia Tech, by Dr. J. Seitzman, and by Dr. P.K. Yeung.

#### References

1. Williams, F.A., *Combustion Theory*, 2<sup>nd</sup> Ed., Addison-Wesley, New York, 1985, pp. 411-437.
2. Menon, S., and Chakravarthy, V. K., *Large-Eddy Simulations of Premixed Flames in Couette Flow*, 32<sup>nd</sup> AIAA/ASME/SAE/ASEE Joint Propulsion Conference, Lake Buena Vista, FL, July 1996.
3. King, M.K., "Overview: NASA Microgravity Combustion Science Program," *Proceedings of the Third international Microgravity Combustion Workshop*, 1995, pp. 3-8.
4. Aydin, E. M., and Leutheusser, H. J., "Plane-Couette flow between smooth and rough walls," *Experiments in Fluids*, Vol. 11, 1991, pp. 302-312
5. Bech, K.H., Tillmark, N., Alfredsson, P.H., Andersson, H.I., "An Investigation of Turbulent Plane Couette Flow at low Reynolds Numbers," *Journal of Fluid Mechanics*, Vol. 285, 1995, pp. 291-325.
6. El Tebany, M.M.M., Reynolds, A.J., "The Structure of Turbulent Plane Couette Flow," *Journal of Fluids Engineering*, Vol. 104, 1982, pp. 367-372.

7. Robertson, J. M., and Johnson, H. F. (1970), "Turbulence Structure in Plane Couette Flow," *J. Eng. Mech.*, Proc. of Am. Soc. of Civil Engg., Vol. 6, pp. 1171-1182.
8. Lekan, J., Gotti, D.J., Jenkins, A.J., Owens, J.C., Johnston, M.R., "User Guide for the 2.2 Second Drop Tower of the NASA Lewis Research Center," *NASA Technical Memorandum 107090*, 1996.
9. Clark, J.A., "A Study of Incompressible Turbulent Boundary Layers in Channel Flow," *ASME Journal of Basic Engineering*, Vol. 90, 1968, pp.455-468.
10. Pope, S.B., *Turbulent Flows (Draft of Chapter 1-7)*, to be published, pp. 249-274.
11. Hinze, J.O., *Turbulence*, 2<sup>nd</sup> edition, McGraw-Hill, New York, 1987, pp.44-48.